Journal of Power Sources xxx (xxxx) xxx–xxx

Contents lists available at ScienceDirect

Journal of Power Sources

journal homepage: www.elsevier.com/locate/jpowsour

Effect of overcharge on $Li(Ni_{0.5}Mn_{0.3}Co_{0.2})O_2$ cathodes: NMP-soluble binder. II — Chemical changes in the anode

Ira Bloom[a,*], Javier Bareño[a], Nancy Dietz Rago[a], Fulya Dogan[a], Donald G. Graczyk[b], Yifen Tsai[b], Seema R. Naik[b], Sang-Don Han[a], Eungje Lee[a], Zhijia Du[c], Yangping Sheng[c], Jianlin Li[c], David L. Wood III[c], Leigh Anna Steele[d], Joshua Lamb[d], Scott Spangler[d], Christopher Grosso[d], Kyle Fenton[d]

[a] Chemical Sciences and Engineering Division, Argonne National Laboratory, Argonne, IL 60439, USA
[b] Analytical Chemistry Laboratory, Nuclear Engineering Division, Argonne National Laboratory, Argonne, IL 60439, USA
[c] Energy and Transportation Science Division, Oak Ridge National Laboratory, Oak Ridge, TN 37831, USA
[d] Power Sources Technology Group, Sandia National Laboratories, Albuquerque, NM 87185, USA

HIGHLIGHTS

- Cells were systematically overcharged and the resulting components, characterized.
- Cathode metals were found in anode; their concentrations increased with state-of-charge.
- Anode surface chemistry indicates a mixture of $LiF:LiPO_3$ and organophosphates.
- The area ratio of the two of the organophosphates tended to a steady state with SOC.

ARTICLE INFO

Keywords:
Lithium-ion battery
Overcharge
SEI layer

ABSTRACT

Cells based on nickel manganese cobalt oxide (NMC)/graphite electrodes, which contained polyvinylidene difluoride (PVDF) binders in the electrodes, were systematically charged to 100, 120, 140, 160, 180, and 250% state of charge (SOC). Characterization of the anodes by inductively-coupled-plasma mass spectrometry (ICP-MS), X-ray photoelectron spectroscopy (XPS), and high-performance liquid chromatography coupled with electrospray ionization mass spectrometry (HPLC-ESI-MS) showed several extent-of-overcharge-dependent trends. The concentrations (by wt) of nickel, manganese, and cobalt in the negative electrode increased with SOC, but the metals remained in the same ratio as that of the positive. Electrolyte reaction products, such as $LiF:LiPO_3$, increased with overcharge, as expected. Three organic products were found by HPLC-ESI-MS. From an analysis of the mass spectra, two of these compounds seem to be organophosphates, which were formed by the reaction of polymerized electrolyte decomposition products and PF_3 or $O=PF_3$. Their concentration tended to reach a constant ratio. The third was seen at 250% SOC only.

1. Introduction

A lithium-ion cell usually consists of a layered, lithiated transition-metal oxide as the cathode, an electrolyte, which is a mixture of organic carbonates and a lithium-bearing salt, and a graphite negative electrode. Probably the most important part of lithium-ion cells is the surface of the electrode. It affects the performance [1] and, possibly, the abuse response of the cell. In normal operation, the electrode reacts with the electrolyte, forming a passivating or solid electrolyte interphase (SEI) layer. At the positive electrode, the SEI layer consists of electrolyte oxidation products and, at the negative, electrolyte reduction products [2–4]. The structure and composition of the SEI is complex under normal operating conditions [5–9]. However, the changes in the SEI layers during overcharge are not well-understood. There are very few reports about what changes occur during the overcharge condition. Logically, one would expect that these changes would depend on the electrode binder and cell chemistry. Characterization of cells after overcharging would be very useful from the safety view point. The information gained may help mitigate the consequences of overcharge by telling us the nature of the SEI, how it changes during

* Corresponding author.
E-mail address: ira.bloom@anl.gov (I. Bloom).

https://doi.org/10.1016/j.jpowsour.2017.12.015
Received 14 September 2017; Received in revised form 5 December 2017; Accepted 7 December 2017

overcharge, and, possibly, how to increase its robustness.

Argonne National Laboratory (Argonne), Oak Ridge National Laboratory (ORNL), and Sandia National Laboratories (SNL) are collaborating to understand the physical and chemical changes on and in the electrodes that occur during cell abuse, such as during overcharge and overheating. The parameters in this study are the effects of the binder in the electrodes and of cell chemistry on the response of the cell to abusive conditions.

The first part of the study investigated the changes in the cell that were from the stepwise overcharge of $Li(Ni_{0.5}Mn_{0.3}Co_{0.2})O_2$ (NMC532)/graphite cells made with the *N*-methylpyrrolidinone (NMP)-soluble binder, poly(vinylidene difluoride) (PVDF). Here, the cells were charged to 100–250% SOC (overcharged 0–150%). After overcharge, the cells were discharged to 0% SOC and taken apart in an argon-filled glovebox. These results were divided into three related papers, described below.

The first paper described the changes in the surface morphology of the anode. Here, scanning-electron microscopy (SEM) and energy-dispersive spectroscopy (EDS) were used [10a]. In that study, the copper foil current collector under the anode layer displayed two sides; a dull side with exposed Cu grain boundaries and a smooth side with the typical microstructure of rolled copper. During cell disassembly, the anode layer exhibited more delamination from the collector on the shiny side (Fig. 1), most likely due to poor binder adhesion to the smooth surface.

In the first paper we found that, starting at 140% SOC, dendrites, such as those shown in Fig. 1, and transition metals were seen on the anode surface. Their concentrations increased with SOC. Additionally, their microstructure was very heterogeneous. In some places, it displayed a complex, layered structure.

This paper, the second in the series, provides a more detailed delineation of these surface materials and the bulk anode to further understand the chemical nature of the observed changes in the anode, the trends in these changes, and, possibly, the processes that led to them. Inductively-coupled-plasma mass spectrometry (ICP-MS), X-ray photoelectron spectroscopy (XPS), and high-performance liquid chromatography (HPLC) were used.

Finally, the third paper describes the changes at the cathode of these cells. Here, XPS, SEM, EDS, ^6Li nuclear magnetic resonance spectroscopy, and X-ray diffraction analysis of the cathodes indicated the formation of a thin, carbon- and oxygen-rich interfacial layer on the cathode surface and lithium loss above 140% SOC. However, the layered crystal structure was retained throughout the experiment [10b].

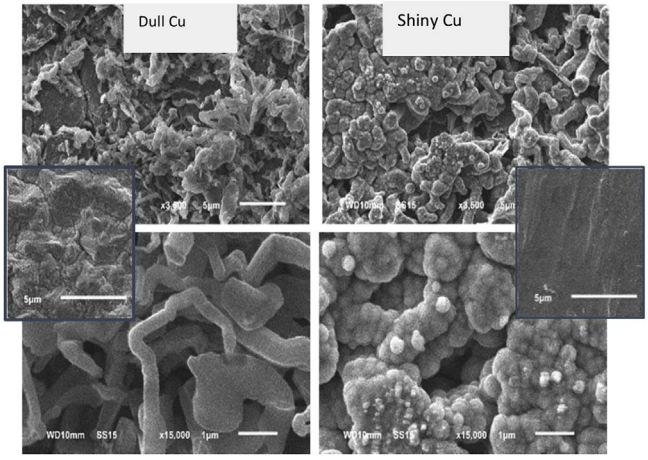

Fig. 1. The insets show the surface morphologies of the copper foil under the graphite layer. Well-defined copper grains were seen on the dull side; grain boundaries were not obvious on the shiny side. The larger images show the surface morphologies on an anode taken from a cell overcharged to 140% SOC. The morphology of the dull side consisted of cylindrical, dendrite-like structures. The structures on the shiny side were nodular (from Ref. 9a).

2. Experimental

Materials. 1.5-Ah lithium-ion cells containing NMC532/graphite chemistry were fabricated, formed, and overcharged, as described in a previous publication [10a]. The rated capacity corresponded to about 55% of the theoretical amount of lithium in the oxide. The NMC532 cathode and graphite anode contained the NMP-soluble binder, PVDF. The negative-to-positive ratio was 1.1:1. With the exception of the outer two layers, all electrodes were double-sided. The electrolyte consisted of 1.2 M $LiPF_6$ in ethylene carbonate:diethylcarbonate (3:7 by wt). Further information is given in Ref. [10a].

3. Post-test characterization

As described earlier [10a], in an argon-filled glovebox, the cells were opened using ceramic scissors. The electrodes were removed from the separator ribbon and allowed to dry. Sections of the separator and positive and negative electrodes were cleaned by swirling them two times in excess dimethylcarbonate for 1 min each. After drying, the sections were characterized using elemental analysis, XPS, and HPLC.

ICP-MS. In the glovebox, the electrode coatings were scraped off the foils onto glassine paper using a spatula. Care was taken to keep the materials from each side of the anode laminate separate.

In the analysis process, each sample was first heated in air to burn off the carbon/organic components. For this step, a 100-mg portion of the sample material was transferred to a weighed quartz beaker (25 mL) and weighed. Then the beakers were placed in a laboratory furnace and heated in stages at 250, 500, and 700 °C. The temperature at each setting was held for several hours with at least four hours at 700 °C to ensure complete removal of graphitic carbon. The beakers were cooled in air.

The residue from ignition was dissolved by adding to the quartz beakers a small amount of water (enough to wet the residue), 3 mL Optima Grade HCl, and 2 mL Optima Grade nitric acid; covering the beaker with a watch glass; and heating under reflux. Each resulting solution was quantitatively transferred to a polypropylene centrifuge cone and diluted with water to 50 mL. The anode solutions were analyzed with a Perkin Elmer/Sciex ELAN DRC-II ICP-MS to determine concentrations of Ni, Mn, and Co, using either scandium or indium as the internal standard. The inductively coupled plasma mass spectrometer (ICP-MS) was calibrated with solutions prepared by diluting spectroscopic standards procured from Ultra Scientific, North Kingstown, RI. The mass fraction (μg/g) of each element in the anode material was calculated using the element concentration, the volume of solution in which the sample was dissolved, and the mass of sample taken. Uncertainty in the reported values is assigned as the larger of ± 1 μg/g or ± 6% of the reported value.

X-ray photoelectron spectroscopy (XPS). XPS of rinsed electrodes was conducted in a PHI 5000 VersaProbe II system from Physical Electronics with a base pressure of $\sim 2 \times 10^{-9}$ torr. The system was attached to the Ar- atmosphere glovebox and the samples were inserted into the XPS analysis chamber through the glovebox without exposure to ambient air. The spectra were obtained using an Al Kα radiation ($h\upsilon$ = 1486.6 eV) beam (100 μm, 25 W), with Ar+ and electron beam sample neutralization, in Fixed Analyzer Transmission mode with a pass energy of 11.75 eV. Shirley background subtraction and fitting to multiple Gaussian peaks were performed on all spectra using the Multipack software from Physical Electronics.

HPLC. Samples for HPLC analysis were prepared by scraping the anode coating (~40–70 mg) off the copper foil from the cells. Care was taken to keep the scrapings from the shiny and dull sides of the copper foil separate. The scrapings were placed in scintillation vials, then covered and removed from the glovebox. Approximately 1–1.5 mL of

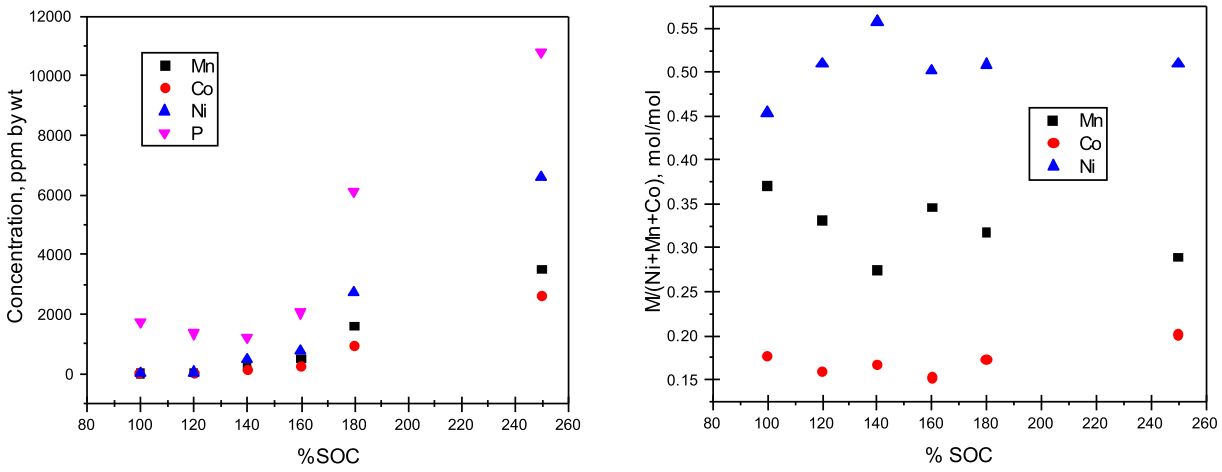

Fig. 2. ICP-MS results from the anode material, with the graph on the left representing ppm by wt and, the graph on the right, mole fraction vs. % SOC. The results are from the dull side of the copper foil.

HPLC-grade water (Sigma-Aldrich) and ~20–30 mg reagent-grade Na_2CO_3 were added to each vial. (A variation of this procedure has been reported by Petibon et al. [11].) After the addition of Na_2CO_3, the pH of the aqueous phase was measured using MColorpHast™ strips (EMD Millipore Corporation).

In some cases, a small number of bubbles formed, indicating the presence of residual lithium. The contents of each vial were mixed thoroughly using a vortex mixer after the bubbling (if any) stopped. Approximately 1–1.5 mL CH_2Cl_2 (Sigma-Aldrich; Chromasolv®) was added to each vial. Again, the contents of each vial were blended thoroughly using the vortex mixer. After the layers separated, the bottom layer was carefully removed using a pipette; placed in an amber HPLC sample bottle; and allowed to dry overnight. The residue was then taken up in ~1 mL acetonitrile (HPLC grade) and capped. The sample bottles were placed in the autosampler.

HPLC analyses were performed using an Agilent Technologies 1260 Infinity chromatograph equipped with an auto-sampler (Agilent Technologies G1329B); a quaternary pump (Agilent Technologies G1311B); and an electrospray, quadrupole mass spectrometer detector (Agilent Technologies 6120; MSD). The fragmenting voltage in the MSD was 70 V and data were collected in the m/e range of 50–1000 Da. Separations were performed using a Zorbax® ODS column (5 µm, 4.6 × 250 mm), which was thermostated at 25 °C. Water and acetonitrile (both HPLC-grade, Sigma-Aldrich, and containing 0.1% formic acid) were mixed in a 60/40 v/v ratio using the quaternary pump to form the mobile phase. The pumping speed was 1 mL min^{-1}. The column was purged with the mobile phase for 5–10 min before using.

Windowed, evolving factor analysis (WEFA) [12–17] was performed using HPLC data to determine the number of discreet components present when there was an overlap of the peaks in the chromatogram. For this work, the m/e values for each time increment were arranged as n columns and 5500 rows in an Excel® worksheet, where 10 × m/e was the row index in each column in the worksheet. If no data were present for a given value of m/e, zero was assigned to that cell. In the discussion that follows, this will be referred to as the data matrix, **D**. The eigenvalues of **D** were calculated using routines written in Visual Basic for Applications in Excel® [18]. The eigenvalues were then used to determine the minimum number of components that would adequately describe the data. It was assumed that the response of the MSD was a linear combination of the individual components present.

In Microsoft® Excel®, baseline correction of the retention time data was performed by subtracting a constant, representing the apparent offset from the x-axis (see appendix for more details). The resulting retention time data from the MSD were approximated using a series of Gaussian curves, which formed the concentration vs. time curve for each component in the sample, where the number of pure components was determined by using the results from WEFA. The true concentration vs. time curves were determined by target transform factor analysis [12,13]. The estimated mass spectrum of each component was calculated by least-squares fitting of the concentration curves to the data. These calculations are described in the appendix.

The estimated mass spectrum was used to determine the molecular ion for each component. The single-ion chromatograph (abundance vs. time) was constructed for this ion and was used to further refine the calculated mass spectrum using the methods described earlier.

The area under the Gaussian curves was calculated by Simpson's rule. These values served as estimates of the area under the retention time curve for each component. The estimated error in the area calculation was on the order of 3–5%.

All carbon-containing organic compounds are expected to display peaks due to the incorporation of ^{13}C in their structures. The general approach was to estimate the number of carbons in a molecule from the ratio of the areas under the m and $m+1$ peaks in the mass spectrum. Since the natural abundance of ^{13}C is $p \sim 1.1\%$, in a molecule containing N carbon atoms, the intensity of the m peak is proportional to the probability of picking all ^{12}C atoms, when drawn randomly. The same is true regarding the intensity of the $(m+1)$ peak regarding the probability of picking one ^{13}C atom. The ratio of these peak areas, R, is therefore $R = N\frac{p}{1-p}$. Or, $N \approx 89.91R$. The estimated error in this calculation was ~10%.

4. Results

ICP-MS. From Fig. 2, the concentration by weight of phosphorus and all transition metals found at the anode increased dramatically with the % SOC. Even at 100% SOC, small concentrations of these elements were evident. The concentrations of transition metals were greater on the dull side than on the shiny side by a factor of about 2 in the SOC range of 120–180%.

Converting the data in Fig. 2 to molar ratios shows that the mole fractions of the metals, M/(Ni + Mn + Co), in the anode echoed that of the cathode material. They were all 5:3:2 for Ni, Mn, and Co, respectively, within experimental error. These results indicate that, as SOC increased, the concentrations of metals also increased, but that no metal was transported preferentially.

The results from the shiny side displayed the same trends, but the concentrations of the species (ppm by wt) were smaller. The M/(Ni + Mn + Co) ratios vs. %SOC on the shiny side were similar to those on the dull side.

XPS. Fig. 3 contains plots of the XPS spectra from the anode (shiny collector side) harvested from discharged cells after overcharging to

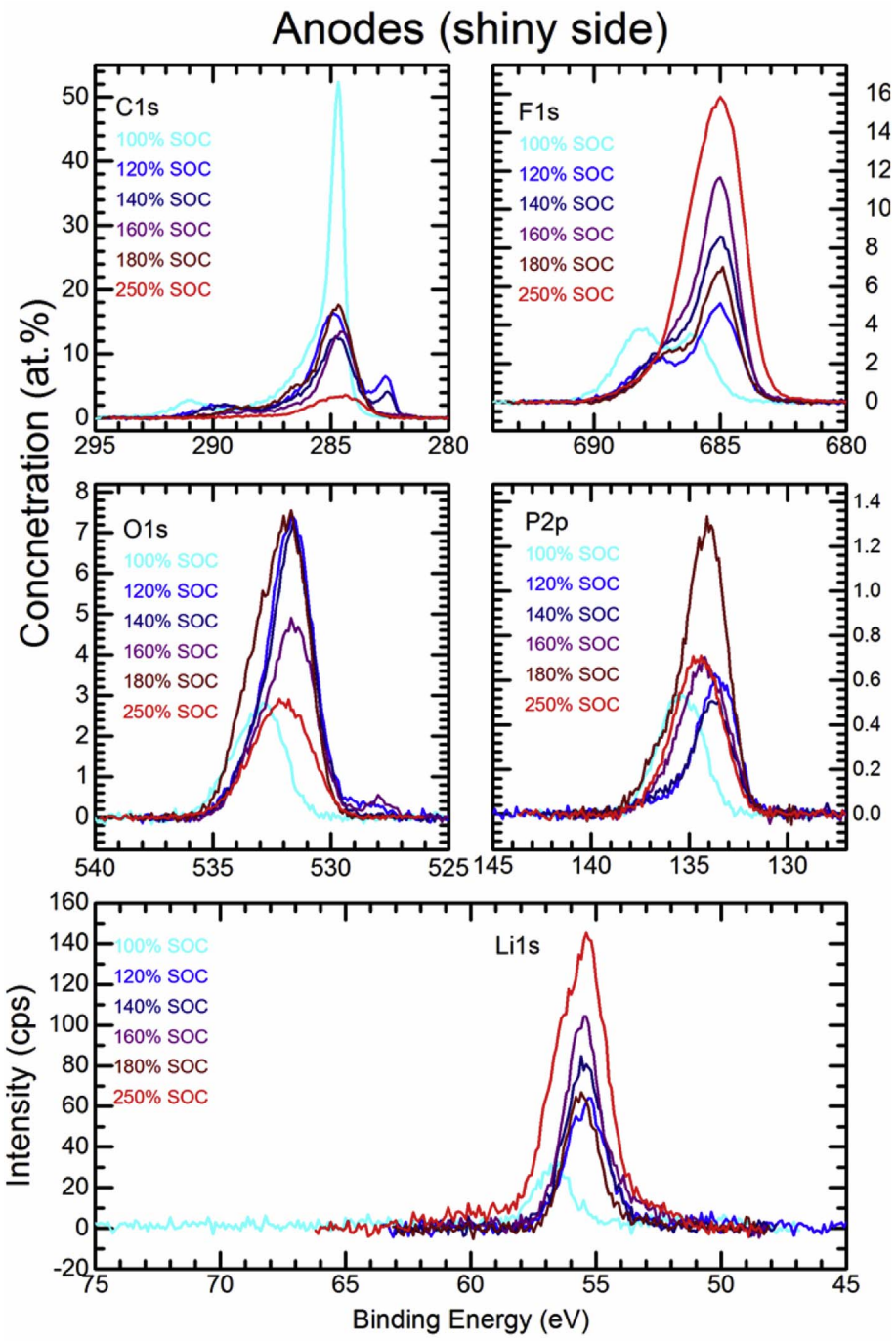

Fig. 3. XPS spectra of harvested anodes on the shiny current collector side. C1s, F1s, O1s, and P2p regions were scaled by the appropriate relative sensitivity factors so the vertical axis is proportional to the atomic concentration. The low binding energy region (bottom panel) was not scaled, so its vertical axis corresponds to the detected photoelectron intensity.

Table 1
Atom percent compositions of the examined anodes (on the shiny side of the current collector), determined by XPS.

	100% SOC	120% SOC	140% SOC	160% SOC	180% SOC	250% SOC
C1s	68.09	45.96	35.37	28.41	39.4	9.64
F1s	14.51	14.77	22.57	27.44	16.97	44.13
Li1s	8.46	18.44	23.31	28.36	18.81	35.23
O1s	7.4	19.13	17.32	13.67	20.95	8.8
P2p	1.55	1.69	1.43	2.12	3.87	2.2

Table 2
Labels for the peaks in the HPLC results, found m/e, and estimated number of carbon atoms.

Retention time, min	Label	Found m/e, Da	Estimated number of carbons
2.76	A	419	17.6
6.53	B	445	12.7
3.14 (250% SOC only)	C	373/351	Unidentified

100% SOC (no overcharge), 120% SOC, 140% SOC, 160% SOC, 180% SOC, and 250% SOC. XPS spectra were acquired in the C1s, F1s, O1s and P2p regions, as well as in the low binding energy region containing the Li1s peak. The ordinate axis for the C1s, F1s, O1s, and P2p regions has been scaled by the relative structure factor (RSF) of each element to reflect atomic concentration (at.% eV^{-1}). This scaling is not possible in the low binding energy region spectrum due to the presence, and potential overlap, of peaks corresponding to different elements with dissimilar RSF; therefore, the ordinate axis for this region reflects XPS signal intensity (counts per second).

The atomic composition of the anode surface, as determined by XPS, is given in Table 1. These compositions are determined by comparing the areas under each elemental region, which were determined by fitting a sum of Gaussian peak shapes to each region. The parameters of these fits, as well as element attribution and relative concentration, are given in the supplementary table, XPS-Sup-1 (see Appendix). These tables list both the originally measured binding energy (BE) and corrected (BE + ϕ) binding energies for each component, as well as the binding energy correction factor (ϕ). The determination of ϕ for each spectrum is based on its interpretation as follows.

An examination of the total concentration of F and Li in the anode sample series (see Fig. 4) indicates a linear relationship with a slope close to one. This dependence suggests that the main process for the increase in F and Li concentrations at the anode is the incorporation of LiF to the growing surface film. Following this hypothesis, we determined the values of ϕ that place the apex of the F1s peak at 685.0 eV, where LiF is expected [19]. This correction places the centroid of all the Li1s peaks in the anode series between 55.4 eV and 55.6 eV, close to the 55.7 eV BE expected for Li in LiF [19]. For most anodes this correction also results in a good overall alignment of the C1s, O1s, and P2p regions. The exception is the spectrum corresponding to the 100% SOC anode (cyan line). In this case, the BE correction based on assigning the low BE component of the F1s spectrum to LiF results in a C1s spectrum residing at too low BE, with the sharp (main) C1s component peaking at 283.6 eV. For this electrode the preferred ϕ was obtained by attributing the small C1s peak at high BE to CF environments in the PVDF binder [20], and shifting it to the 290.9 eV BE observed in the cathode series [10b]. This adjustment places the main C1s component at 284.7 eV, consistent with CH environments in a variety of organic molecules and in line with the dominant component of the C1s spectra of the other anodes examined.

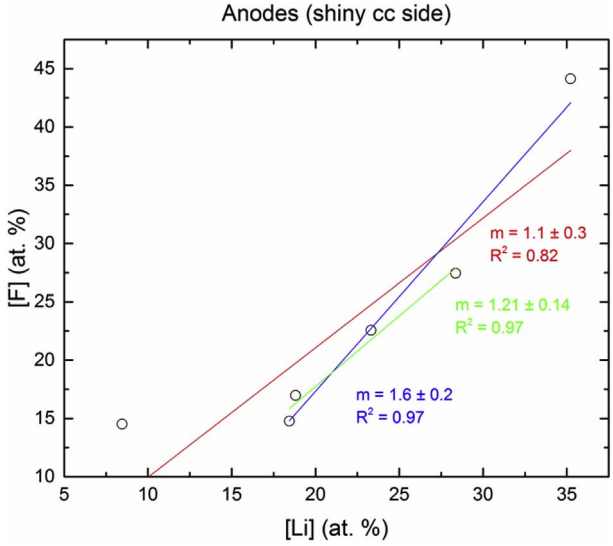

Fig. 4. Plot of atomic concentration of F v. Li in the anodes, determined by XPS. Different color lines are linear regressions of the data points spanned by the lines, with their respective slopes (m) and regression coefficients (r^2) indicated. (For interpretation of the references to color in this figure legend, the reader is referred to the Web version of this article.)

The positions and shapes of the F1s, O1s, P2p, and Li1s peaks suggest the presence of a substantial amount of LiF:$LiPO_3$ in the anode SEI. The F1s spectra between 120% SOC and 180% SOC have two clearly resolved components peaking around 685 eV and 687–687.5 eV. While the 685 eV component is consistent with LiF, as stated above, the F1s region of LiF:$LiPO_3$ is also expected to have two components: one centered between 684.4 eV and 684.9 eV, and another between 687.0 eV and 687.5 eV, depending on the LiF content [21]. Additionally, the O1s peaks are observed at around 531.5 eV and the P2p peaks at around 134 eV, while the corresponding peaks in LiF:$LiPO_3$ occur around 4531.1–531.5 eV and 133.8–134.3 eV, respectively. Li 1s in LiF:$LiPO_3$ shows up between 55.1 eV and 55.4 eV. Consequently, the observed Li1s range between 55.4 eV and 55.6 eV falls between Li-F:$LiPO_3$ and LiF (55.7 eV). Although the contributions from LiF (by itself) and LiF:$LiPO_3$ to the observed Li1s and F1s spectra are not clearly resolved, it is clear that the total amounts of Li and F in the anode samples (F/P ratios ranging between ~4 and 20) are much higher than would be expected for LiF:$LiPO_3$. However, with the exception of the 100% SOC sample the Li/F ratios are all very close to 1 (1.25, 1.03, 1.03, 1.11, and 0.80 for 120% SOC, 140% SOC, 160% SOC, 180% SOC, and 250% SOC, respectively). Together with the observation that at a higher SOC the 685 eV F1s contribution (common to LiF and LiF:$LiPO_3$) becomes more dominant, these observations suggest that the formation of LiF is the dominant mechanism of incorporation of Li and F into the anode SEI, with some formation of $LiPO_3$, especially at a lower SOC. It is also worth noting that, with the exception of the 250% SOC sample, the relative concentration of P in the anode SEI is much higher than in the cathode surface film (between 2.6 and 4.9 times).

As indicated above, the C1s spectra from the anode series are dominated by CH contributions at around 285 eV BE. As the SOC increases, the overall C content in the samples decreases and the CH contribution broadens, extending to a lower BE. The high BE tails of the CH contributions to the C1s spectra extend into the 286 eV range typical of CO contributions (e.g., poly(phenylene oxide)) at 285.9 eV [22]. Additionally, there is some intensity around 289–290 eV where both carbonate (e.g., Li_2CO_3 C1s at 289.55 eV [23]) and CF environments (e.g., C_6F_6 C1s at 289.0 eV [24]) appear, which decreases at increasing SOC's and disappears completely in the 250% SOC electrode. Finally, a low BE peak around 282.7 eV is present in the 120% SOC and 140% SOC samples. This peak is consistent with Li trapped in CH-rich compounds (e.g., $LiCH_3$ at 282.4 eV [25]).

In contrast to the ICP-MS analysis, no transition metals were detected at the anode by XPS. This suggests that the transition metals may be buried under the more organic layer(s) detected by XPS or that the total concentration of the transition metals in the anode SEI was below XPS detection limits (~1 at%).

HPLC. To understand the nature of the surface materials observed in the scanning electron microscope (SEM), samples of anode materials were hydrolyzed. The CH_2Cl_2 extract from the hydrolysis was then analyzed using the HPLC. Fig. 5a shows plots of the total ion count (abundance) vs. time from the mass spectrometer detector from materials harvested from the dull side. A similar analysis using approximately the same amount of material from the shiny side of the foil yielded analogous trends, but the overall response of the detector was lower, indicating lower concentrations of dissolved species. For the sake of simplicity, the remaining discussion will be limited to those materials

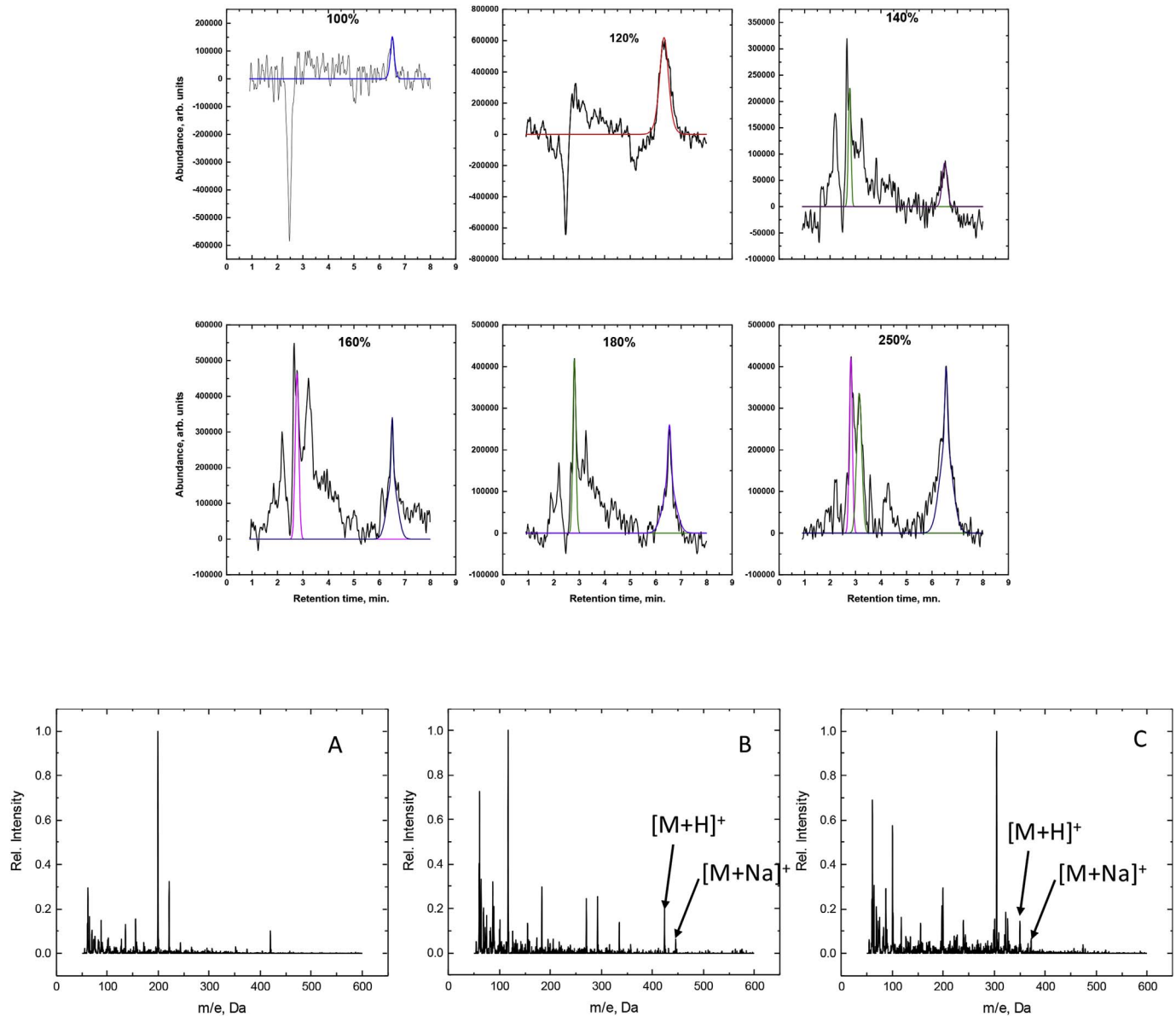

Fig. 5. a. HPLC results from the methylene chloride extract from hydrolysis of the materials on the anode surface from the dull side of the copper foil. The number given on each plot is the %SOC to which the cell was charged. In some cases, the MSD response was negative. Analysis indicated that these responses represented noise, not actual data. They were omitted from further consideration. The colored curves represent the Gaussians used to estimate the area under each curve, after removing any remaining offset in the *y* direction. See supplementary information for more details. The peaks without colored, Gaussian curves are from the column. b. Calculated, refined mass spectra corresponding to the retention times shown in Table 2.

observed from the dull side.

Examining the chromatograms shown in Fig. 5a revealed that some of the peaks overlap. Portions of the factor analysis process [12–17] were used to deconvolute them into independent Gaussian curves. A detailed description of all the results from this process is beyond the scope of this paper. Interested readers are encouraged to peruse references [12,13]. These Gaussians were then used to calculate the crude mass spectrum.

After identifying promising candidate peaks in the crude spectrum, individual ion chromatograms were constructed if the peak had a corresponding ^{13}C isotope peak. This resulted in two curves, one for the m/e value and another for the $(m+1)/e$ value. These ion concentration curves were used to refine the mass spectrum using the principles alluded to above. Additionally, using the areas in the refined mass spectrum was thought to yield better results than using the area under the curve in the chromatogram or under peaks in the crude mass spectrum. The area under the curve in the chromatogram can be from two or more species that co-elute and, thus, the other species will confound the mass spectrum of the species of interest and the subsequent calculations.

The organic compositions described below were derived assuming that the observed maximum-mass peak represented (m+1)/e. The compositions were based on those proposed or observed in the literature, such as those based on the free-radical-induced decomposition and polymerization of ethylene carbonate and the interactions of electrolyte decomposition products [3,7,25–44].

The calculated mass spectra corresponding to the retention times shown in Table 2 are shown in Fig. 5b. A close examination of the spectrum for Peak A showed that m/e peak was at 419 Da, and, as expected, its companion ^{13}C peak was at 420 Da. The number of carbons in the compound corresponding to Peak A was 17.6 based on the area ratio of these peaks, as shown in Table 2.

If we include the 10% error around the above value of 17.6, we find that there can be between about 16 and 19 carbon atoms in the compound. Thus, we investigated the possible compounds with between 16 and 19 carbon atoms which may be formed from the polymerization of

the organic carbonates and subsequent reaction either PF_3 or $O=PF_3$. We limited this investigations to potential compositions that yielded reasonable molecular structures. The result was two promising candidates, $C_{16}H_{36}O_{10}P^+$ (FW = 419.42 g mol^{-1}) and $C_{18}H_{38}O_6PF_2{}^+$ (FW = 419.46 g mol^{-1}). The structures of the potential compounds, as neutral molecules, are shown in Structures 1 and 2, respectively.

$HOCH_2CH_2OCH_2CH_2OP(=O)(OCH_2CH_2OCH_2CH_2OCH_2CH_3)_2$ Structure 1

$F_2P(=O)OCH_2CH_2OCH_2CH_2OCH_2CH_2OCH_2CH_2OC_{10}H_{21}$ Structure 2

Examination of Structure 1 shows that it consists of fragments which are from the organic carbonates, such $-OCH_2CH_2O-$ and $-OCH_2CH_3$, which reacted with PF_3 or $O=PF_3$. If the reaction was with PF_3, one would expect a phosphite. The oxidation of the phosphite to phosphate most likely could have happened during the hydrolysis step, which was performed in air. Compounds of this type have been reported in the literature [45a-c].

Structure 2 may be more problematic. It contains molecular fragments from the organic carbonates, but also has a long aliphatic terminus, $-C_{10}H_{21}$. Conceivably, this aliphatic group could be formed by the free-radical polymerization of $CH_2=CH_2$, another postulated product from the reduction of EC [39]. However, the probability of a long, strictly aliphatic chain may be low. Structure 1 may, therefore, be more likely and a more reasonable candidate.

A similar analysis of the mass spectrum for Peak B was slightly more complex. There were two peaks in the refined mass spectrum that could be due to the molecular ion, 423 and 445 Da. The difference between them, 22 Da, could be due to the incorporation of H^+ ($[M+H]^+$) in the former and Na^+ ($[M+Na]^+$) in the latter. Namely, if the former peak was due to the protonation of a species with a molecular weight of 422 g mol^{-1}, adding H^+ or Na^+ to it would yield species consistent with the observations. The most likely source of sodium was the Na_2CO_3 used in sample preparation. The number of carbon atoms in the compound was 12.7 based on the ratio of the area under the ^{13}C peak to that for the ^{12}C peak in the mass spectrum.

Similar to Peak A, we investigated compounds with between 11 and 14 carbon atoms for Peak B. We assigned Structure 3 (FW = 422.30 g mol^{-1}) to represent the neutral compound corresponding to Peak B. A possible route to the 3-carbon side chain on one of the phosphorus atoms is described in the Discussion section.

$$\mathrm{HOCH_2CH_2O\underset{\substack{|\\ OCH_2CH_2OH}}{P}(=O)OCH_2CH_2OCH_2CH_2O\underset{\substack{|\\ OCH_2CH_2CH_3}}{P}(=O)OC_2H_5}$$

Structure 3

A new species appeared in the analyte from the 250% SOC cell, compound C, which had an m/e peak at 373 Da. An analysis of its mass spectrum showed clear evidence of a peak at 374 Da. The number of carbon atoms in this compound based on the ratio of the areas of these peaks is 6.2. A close examination of the mass spectrum showed that there was also a peak at 351 Da, indicating the peaks were most likely due to $[M+H]^+$ and $[M+Na]^+$ ions. Analogous to compound B, compound C may contain phosphate/ether/carbonate functional groups. However, the formula of this compound remains unknown.

The relative areas of Peaks A and B vs. %SOC are plotted in Fig. 6. From Fig. 6, there were obvious trends in these data. At low values of % SOC, only Peak B was observed. As %SOC increased past 120%, Peak A grew in and Peak B decreased. The peaks then were present in a constant area ratio, ~4.5:1.

5. Discussion

As the cells were charged to higher and higher levels, it was interesting to note that the transition metals — Ni, Mn, and Co — were transported to the anode in the same molar ratio as that found in the cathode, 5:3:2, respectively. Their concentrations increased with an increasing overcharge. The transport of these metals has been reported by others. For example, Yuan, et al. [46] overcharged 32-Ah cells containing $LiNi_{1/3}Mn_{1/3}Co_{1/3}O_2$ cathodes and observed a similar effect: the metals were transported to the anode in the same ratio as that of the cathode material when the cell was charged to 100–200% SOC. It is likely that, as the cathode is charged to higher voltages, there is less lithium to carry the charge. Other components of the cathode may participate, assuming the effective charge on these metals is about +3.

Fig. 6. Relative areas of peaks in the HPLC results from the dull side of the copper current collector. See Table 2 for a definition of the labels on the curves in the figure.

The dissolution of transition metals from the cathode could be dependent on several factors, such as temperature, particle size and morphology (i.e., surface area). This is likely a complex process; the characterization and understanding of which is outside the scope of this work. Zheng et al. [47], report the trends in metal ion concentration with potential at states of charge less than 100%. The metal concentrations in this range of SOC is relatively low, typically between 0 and 0.25 ppm. These concentrations increase sharply once the cell potential reaches about 4.4 V. The observations were ascribed to the action of HF acting on the cathode.

In the literature [48–53], there have been additional reports of HF forming at high potentials; corroding the cathode surface; and liberating transition metal ions. These cations then can migrate to the anode and deposit. The overcharge experiment described in this work could be thought of as an extreme case of operating a cell at high potentials. Therefore, the trend in transition metal concentration is a reflection of the reported effect of HF on the cathode.

The XPS and HPLC results show that the SEI on the anode is complex, containing inorganic and organic components. The XPS and elemental analysis results suggest that Li_xPOF_y in the anode SEI increases with an increasing degree of overcharge, which is most likely from electrolyte degradation reactions. Prototypical reactions, such as those given in Refs. [3,25,26] and shown in Eq. (1), illustrate how "Li_xPOF_y," can be generated.

$$\begin{aligned}&LiPF_6 \rightarrow LiF + PF_5\\&PF_5 + \text{residual } H_2O \text{ in electrolyte} \rightarrow POF_3 + 2HF\\&POF_3 + Li\ (\text{from anode}) \rightarrow Li_xPOF_y + LiF\end{aligned} \quad (1)$$

With an increasing degree of overcharge, one would expect a scenario similar to that in Eq. (1) to occur more readily, increasing the amounts (i.e., layer thickness) of Li_xPOF_y and LiF on the anode surface.

The proposed molecule structures for compounds A and B were selected from many compounds that could be present in the chemical system. The proposed structures were selected by applying the following criteria. The parent-ion peak in the mass spectrum was assigned by looking for ones that made chemical sense. This means that each candidate parent-ion peak at mass *m* must have a companion peak at

mass ($m + 1$), assuming that the compounds are carbon-containing organics. In all cases, the parent-ion peak was not the most intense in the spectrum.

Next, the estimated number of carbon atoms, which was calculated from the ratio of the areas of the ($m + 1$) and m peaks, must yield a reasonable result, meaning that the number of carbons atoms, multiplied by 12 must be less than the parent-ion mass value. Further, the difference between the estimated number of carbon atoms × 12 and the parent-ion mass peak must be large enough to accommodate the other atoms in the proposed formula. Additionally, the number of candidate parent-ion peaks was further limited by looking for ones that were above a reasonable noise threshold.

Initially, only compound B was observed, possibly indicating that it is easily formed with limited surface lithium. As the %SOC increased, compound A appeared. Eventually, the two compounds had equal propensities to be formed. This implies that more surface lithium may be needed to form Compound A and that, after this threshold lithium concentration has been reached, compounds A and B have the same potential to form. Given that the negative:positive ratio was 1.1 implies that one would expect lithium plating above 110% SOC. The fact that compound A appears at 140% SOC supports the hypothesis that more surface lithium was needed for it to form. It was a higher electrolyte polymer.

From the above observations, it is likely that compounds A and B are formed by the free-radical reduction of EC and DEC and the reaction of these fragments with each other and with the salt. Possible structure for these compounds A and B were shown above. These compounds can be formed by using reaction schemes outlined by Aurbach et al. [39]. For example, using Aurbach's scheme regarding ethylene carbonate (EC) [39], $2EC + 2\,Li^+ + 2e^- \rightarrow CH_2{=}CH_2 + (CH_2OCO_2)Li$ and adapting another to the solvent system in this study, $CH_3CH_2OCO_2CH_2CH_3 + Li^+ + e^- \rightarrow CH_3CH_2OCO_2Li + CH_3CH_2\cdot$ or $CH_3CH_2OCO\cdot + CH_3CH_2OLi$, one can easily envision a path for the formation of compound A, such as that shown below in Eq. (2).

$$4\ {}^{\cdot}OCH_2CH_2O^{\cdot} + CH_3CH_2O^{\cdot} + PF_3 + 3Li^+ + H^+ \rightarrow A + 3LiF \qquad (2)$$

Polyethers with longer or an odd number of carbons, such as one of the side chains in compound B, require that a hydrocarbon homologation process operate. A possible method to generate an odd-number of carbons in the hydrocarbon chain is shown in Eq. 3. The nascent methyl radical would also be available for further reactions and may be the source of the odd number of carbons in some of proposed phosphates.

$$CH_3CH_2\cdot \;\rightleftharpoons\; CH_3CH_2OR \longrightarrow CH_3\cdot + CH_3CH_2CH_2OR \qquad (3)$$

The diphosphite could be formed by analogy to the path for compound A, except using two molecules of PF_3 (or $O{=}PF_3$) as the phosphorus source.

Taking the above results together provides a more-detailed picture of the nature of the layers observed in the first paper in the series [10a]. The surface material consisted of organic and inorganic materials, which were most likely due to electrolyte decomposition reactions, that also contained some transition metals.

6. Conclusion

Cells based on NMC/graphite, containing PVDF binders in the positive and negative electrodes, were systematically charged to 100, 120, 140, 160, 180, and 250% SOC. Characterization of the anodes by ICP-MS, XPS, and HPLC showed several extent-of-overcharge-dependent trends. The concentrations (by wt) of nickel, manganese, and cobalt in the negative electrode increased with SOC, but the metals remained in the same ratio as that of the positive. Electrolyte reaction products, such as LiF:$LiPO_3$, increased with overcharge, as expected. Three organic products were found by HPLC-ESI-MS. From an analysis of the mass spectra, two of these compounds seem to be organophosphates, which were formed by the reaction of polymerized electrolyte decomposition products and PF_3 or $O{=}PF_3$. Their concentration tended to reach a constant ratio.

Acknowledgments

We gratefully acknowledge support from the U.S. Department of Energy, Office of Energy Efficiency and Renewable Energy, Vehicle Technologies Office. Argonne National Laboratory is operated for DOE Office of Science by UChicago Argonne, LLC, under contract number DE-AC02-06CH11357.

The work at Oak Ridge National Laboratory was sponsored by U.S. Department of Energy (DOE), Office of Energy Efficiency and Renewable Energy, Vehicle Technologies Office, Applied Battery Research. Oak Ridge National Laboratory is managed by UT Battelle, LLC, for the U.S. Department of Energy under contract DE-AC05-00OR22725.

Sandia National Laboratories is a multi-mission laboratory managed and operated by National Technology and Engineering Solutions of Sandia, LLC., a wholly owned subsidiary of Honeywell International, Inc., for the U.S. Department of Energy's National Nuclear Security Administration (NNSA) under contract DE-NA0003525.

The U.S. government retains for itself, and others acting on its behalf, a paid-up nonexclusive, irrevocable worldwide license in said article to reproduce, prepare derivative works, distribute copies to the public, and perform publicly and display publicly, by or on behalf of the government.

Appendix A. Supplementary data

Supplementary data related to this article can be found at http://dx.doi.org/10.1016/j.jpowsour.2017.12.015.

References

[1] L. Gireaud, S. Grugeon, S. Pilard, P. Guenot, J.-M. Tarascon, S. Lareulle, Anal. Chem. 78 (2006) 3688–3698.
[2] M. Morita, O. Yamada, M. Ishikawa, J. Appl. Electrochem. 28 (1998) 209–213.
[3] S.W. Song, G.V. Zhuang, P.N. Ross Jr., J. Electrochem. Soc. 151 (2004) A1162–A1167.
[4] D. Aurbach, J. Power Sources 89 (2000) 206–218.
[5] E. Peled, J. Electrochem. Soc. 126 (1979) 2047.
[6] J.G. Thevenin, R.H. Muller, J. Electrochem. Soc. 134 (1987) 273.
[7] S.J. An, J. Li, C. Daniel, D. Mohanty, S. Nagpure, D.L. Wood, Carbon 105 (2016) 52–76.
[8] D. Aurbach, I. Weissman, A. Zaban, O. Chuzid (Youngman), Electrochim. Acta 39 (1994) 51.
[9] K. Kanamura, H. Tamura, S. Shiraishi, Z.-i. Takehara, J. Electroanal. Chem. 394 (1995) 49.
[10] (a) N. Dietz Rago, J. Bareno, I. Bloom, J. Li, D.L. Wood, III, L.A. Steele, J. Lamb, S. Spangler, C. Grosso, K. Fenton, Effect of overcharge on lithium-ion cells containing $Li(Ni_{0.5}Mn_{0.3}Co_{0.2})O_2$ cathodes: NMP-soluble binder. I. Microstructural changes in the anode (2018) [unpublished manuscript].
(b) J. Bareño, N. Dietz Rago, F.D. Key, D. Graczyk, Y. Tsai, S. Naik, S.D. Han, E. Lee, Z. Du, Y. Sheng, J. Li, D. Wood, L.A. Steele, J. Lamb, S. Spangler, C. Grosso, K. Fenton, I. Bloom, Effect of overcharge on NMP-processed $Li(Ni_{0.5}Mn_{0.3}Co_{0.2})O_2$ / Graphite lithium ion cells with PVDF binder. III — Chemical changes in the cathode (2018) [unpublished manuscript].
[11] R. Petibon, L. Rotermund, K.J. Nelson, A.S. Gozdz, Jian Xia, J.R. Dahn, J. Electrochem. Soc. 161 (2014) A1167–A1172.
[12] E.R. Malinowski, Factor Analysis in Chemistry, third ed., John Wiley and Sons, Inc., New York, 2002.
[13] Y. Piao, Y. Qin, Y. Ren, S.M. Heald, D. Zhou, B.J. Polzin, S.E. Trask, K. Amine, Y. Wei, G. Chen, I. Bloom, Z. Chen, Phys. Chem. Chem. Phys. 16 (2014) 3254–3260.
[14] J.C. Hamilton, P.J. Gemperline, J. Chemometr. 4 (1990) 1–13.
[15] H.R. Keller, D.L. Massart, Chemometr. Intell. Lab. 12 (1992) 209–224.
[16] P.J. Gemperline, J.C. Hamilton, J. Chemometr. 3 (1989) 455–461.
[17] H. Gampp, M. Maeder, C.J. Meyer, A.D. Zuberbuhler, Talanta 32 (1985) 1133–1139.
[18] http://www.quantcode.com/modules/mydownloads/singlefile.php?lid=173.

[19] From NIST database, W.E. Morgan, J.R. Van Wazer, W.J. Stec, J. Am. Chem. Soc. 95 (1973) 751.
[20] From NIST database, S. Dapoz, N. Betz, M.-J. Guittet, A. Le Moel, Nucl. Instrum. Methods Sec. B 105 (1995) 120.
[21] From NIST database, B.V.R. Chowdari, K.F. Mok, J.M. Xie, R. Gopalakrishan, Solid State Ionics 76 (1995) 189.
[22] From NIST database, J.L. Sanda, J.F. Morar, C.A. Kovac, F.J. Himpel, R.A. Pollack, J. Vac. Sci. Technol. A4 (1986) 1046.
[23] From NIST database, S. Contarini, J.W. Rabalais, J. Electron. Spectroscop. Phenom. 35 (1985) 191.
[24] From NIST database, D.T. Clark, D. Kilcast, D.B. Adams, W.K.R. Musgrave, J. Electron. Spectroscop. Phenom. 1 (1972) 232.
[25] G.F. Meyer, M.B. Hall, J.W. Chinn, R.J. Lagow, J. Am. Chem. Soc. 107 (1985) 1413.
[26] A.M. Andersson, D.P. Abraham, R. Haasch, S. MacLaren, J. Liu, K. Amine, J. Electrochem. Soc. 69 (2002) A1358–A1369.
[27] L. El Ouatani, R. Dedryvère, C. Siret, P. Biensan, S. Reynaud, P. Iratçabal, D. Gonbeau, J. Electrochem. Soc. 156 (2009) A103–A113.
[28] D. Bedrov, G.D. Smith, A.C.T. van Duin, J. Phys. Chem. 116 (2012) 2978–2985.
[29] L. Xing, W. Li, C. Wang, F. Gu, M. Xu, C. Tan, J. Yi, J. Phys. Chem. B 113 (2009) 16596–16602.
[30] Y. Wang, P.B. Balbuena, J. Phys. Chem. 106 (2002) 9582–9594.
[31] Y. Wang, P.B. Balbuena, J. Phys. Chem. B 106 (2002) 4486–4495.
[32] Y. Wang, S. Nakamura, K. Tasaki, P.B. Balbuena, J. Am. Chem. Soc. 124 (2002) 4408–4421.
[33] R.L. Sacci, N.J. Dudney, K.L. More, L.R. Parent, I. Arslan, N.D. Browning, R.R. Unocic, Chem. Commun. 50 (2014) 2104.
[34] S.-H. Kang, D.P. Abraham, A. Xiao, B.L. Lucht, J. Power Sources 175 (2008) 526–532.
[35] S. Laruelle, S. Pilard, P. Guenot, S. Grugeon, J.-M. Tarascon, J. Electrochem. Soc. 151 (2004) A1202–A1209.
[36] E. Peled, D. Bar Tow, A. Merson, A. Gladkich, L. Burstein, D. Golodnitsky, J. Power Sources 97–98 (2001) 52–57.
[37] L. El Ouatani, R. Dedryvère, C. Siret, P. Biensan, D. Gonbeau, J. Electrochem. Soc. 156 (2009) A468–A477.
[38] H. Ota, Y. Sakata, A. Inoue, S. Yamaguchi, J. Electrochem. Soc. 151 (2004) A1659–A1669.
[39] D. Aurbach, A. Zaban, Y. Ein-Eli, I. Weissman, O. Chusid, B. Markovsky, M. Levi, E. Levi, A. Schechter, E. Granot, J. Power Sources 68 (1997) 91–98.
[40] D. Aurbach, B. Markovsky, A. Schechter, Y. Ein-Eli, H. Cohen, J. Electrochem. Soc. 143 (1996) 3809–3820.
[41] D. Aurbach, E. Zinigrad, Y. Cohen, H. Teller, Solid State Ionics 148 (2002) 405–416.
[42] M. Gauthier, T.J. Carney, A. Grimaud, L. Giordano, N. Pour, H.-H. Chang, D.P. Fenning, S.F. Lux, O. Paschos, C. Bauer, F. Maglia, S. Lupart, P. Lamp, Y. Shao-Horn, J. Phys. Chem. Lett. 6 (2015) 4653–4672.
[43] M. Tochihara, H. Nara, D. Mukoyama, T. Ykokoshima, T. Momma, T. Osaka, J. Electrochem. Soc. 162 (2015) A2008–A2915.
[44] L. Gireaud, S. Grugeon, S. Pilard, P. Guenot, J.-M. Tarascon, S. Lareulle, Anal. Chem. 78 (2006) 3688–3698.
[45] (a) S. Takeda, W. Morimura, Y.-H. Liu, T. Sakai, Y. Saito, Rapid Commun. Mass Spectrom. 30 (2016) 1754–1762;
(b) V. Kraft, W. Weber, B. Streipert, R. Wagner, C. Shultz, M. Winter, S. Nowak, RSC Adv. 6 (2016) 8–17;
(c) C. Schultz, S. Vedder, M. Winter, S. Nowak, Anal. Chem. 88 (2016) 11160–11168.
[46] Q.F. Yuan, F. Zhao, W. Wang, Y. Zhao, Z. Liang, D. Yan, Electrochim. Acta 178 (2015) 682–688.
[47] H. Zheng, Q. Sun, G. Liu, X. Song, V.S. Battaglia, J. Power Sources 207 (2012) 134–140.
[48] H. Ota, Y. Sakata, A. Inoue, S. Yamaguchi, J. Electrochem. Soc. 151 (2004) A1659–A1669.
[49] Y.-K. Han, J. Yoo, T. Yim, Electrochim. Acta 215 (2016) 455–465.
[50] Y. Zhu, X. Luo, M. Xu, L. Zhang, L. Yu, W. Fan, W. Li, J. Power Sources 317 (2016) 65–73.
[51] J.-G. Han, S.J. Lee, J. Lee, J.-S. Kim, K.T. Lee, N.-S. Choi, ACS Appl. Mater. Interfaces 7 (2015) 8319–8329.
[52] Y.-K. Han, J. Yoo, T. Yim, J. Mater. Chem. 3 (2015) 10900–10909.
[53] C. Peebles, R. Sahore, J.A. Gilbert, J.C. Garcia, A. Tornheim, J. Bareño, H. Iddir, C. Liao, D.P. Abraham, J. Electrochem. Soc. 164 (2017) A1–A8, http://dx.doi.org/10.1149/2.1101707jes.